Slow Surface Acoustic Waves via Lattice Optimization of a Phononic Crystal on a Chip

Si-Yuan Yu,[1,2,3,‡] Ji-Qian Wang,[1,2,‡] Xiao-Chen Sun,[1] Fu-Kang Liu,[1] Cheng He,[1,2,3] Huan-Huan Xu,[1] Ming-Hui Lu,[1,2,3,*] Johan Christensen,[4,†] Xiao-Ping Liu,[1,2] and Yan-Feng Chen[1,2,3]

[1] *National Laboratory of Solid State Microstructures & Department of Materials Science and Engineering, Nanjing University, Nanjing, Jiangsu 210093, China*

[2] *Collaborative Innovation Center of Advanced Microstructures, Nanjing University, Nanjing, Jiangsu 210093, China*

[3] *Jiangsu Key Laboratory of Artificial Functional Materials, Nanjing 210093, China*

[4] *Universidad Carlos III de Madrid, Avenida de la Universidad 30, 28916 Leganes (Madrid), Spain*

(Received 19 October 2020; accepted 21 October 2020; published 2 December 2020)

Strategically reducing the speed of waves, which greatly improves both the energy density and information capacity of carrier signals in space, is a key enabling factor for signal-processing devices. Among these devices, especially in the prosperous wireless communication industry, surface acoustic wave (SAW) devices based on interdigital transducers (IDTs) currently hold an essential status. However, velocity reduction in traditional IDT-based SAW devices can be achieved only by using specific substrate materials that are generally of lower hardness, which inevitably leads to an increase in device size and less-optimal electromechanical coupling coefficients. Here, we demonstrate a technological means of realizing slow on-chip SAWs that is relevant for practical rf signal processing, gyrometers, sensing, and transduction. This method takes advantage of the gradual flattening of a Rayleigh-type dispersion band due to the spatial lattice evolution of a surface phononic crystal. In our experiment, the speed of an ultraslow SAW is measured to be approximately 200 m/s, which is even slower than the speed of sound in air and equivalent to 1/17.4 of the speed of the original Rayleigh waves in $LiNbO_3$. Such ultraslow SAWs may have promising applications in time-dependent SAW modulation, high-sensitivity SAW sensors, and SAW nonlinear even quantum-dynamic systems. Additionally, our technique can be similarly applied to a broad range of other two-dimensional or quasi-two-dimensional wave structures, e.g., in electronic, optical, acoustic, and thermal systems.

DOI: 10.1103/PhysRevApplied.14.064008

I. INTRODUCTION

Slow waves, e.g., slow light and slow sound, are of great interest from both scientific and technological perspectives [1–13]. The ability to slow down waves has two main advantages: (1) as information or signal carriers, slow waves are capable of providing considerable data buffering and enabling better time-domain processing of signals [14–19] in miniaturized devices, and (2) as pumping sources, they can be leveraged to generate high intensities, thus leading to enhanced wave-matter interactions [20–23]. An effective approach for generating slow waves is to use Bloch waves [24] in periodic media, e.g., photonic crystals (PCs) [25–27] or phononic crystals (PnCs) [28–30]. In these artificial crystals, the group velocity of the Bloch waves can be engineered to slow down at specific frequencies, where the slopes of the dispersion curves are relatively small. This behavior is realized in PCs with a number of different configurations, e.g., line-defect modes [31,32], resonant modes [9–11], and Bloch modes near the band edge [33]. However, considerably less attention has been paid to investigating slow-wave phenomena in acoustics. There have been only a very limited number of studies on this subject, which have reported resonant-mode-assisted slow Lamb waves in periodic membranes [11], slow airborne sound in a periodically loaded resonator waveguide [9,10] or in groove-perforated [12] or helical-structured [13] metamaterials, and slow guided modes in a two-dimensional sonic crystal [34] or phoxonic crystal [35] (periodic structures that show simultaneous photonic and phononic bandgaps [36]), among other phenomena. It is important to note that most of these

*luminghui@nju.edu.cn
†johan.christensen@uc3m.es
‡These authors contributed equally to this work.

studies have so far remained on a theoretical level with only a few experimental demonstrations. Also, their performance may suffer from a limited bandwidth and/or a large insertion loss due to (1) relatively high acoustic transmission losses in a fluid system (i.e., air [37] or water [38]) compared with in solids [39], and (2) relatively low energy-conversion efficiency, e.g., the conversion of incident plane-wave modes into two-dimensional line cavity modes [40,41] or resonant modes [42,43], which somewhat diminishes their value in practical applications.

Surface acoustic waves (SAWs), especially the Rayleigh waves predicted by Lord Rayleigh in 1885 [44], are an important class of waves that are commonly utilized in modern wireless communication systems. Controlling SAWs with electroacoustic interdigital transducers (IDTs) [45] enables vital electric-signal-processing functionalities that are difficult to attain solely with all-electrical components. A representative application example is a high-frequency narrow-linewidth bandpass rf filter for isolating different signal channels. Recently, with the rapid development of artificial surface microstructures, such as surface phononic crystals (SPnCs), the ability to manipulate SAW transport [46–52] has been greatly expanded. However, as a key enabling factor for signal-processing functionalities, an experimental demonstration of slow SAWs is still missing.

Here, we present a systematic investigation of the acoustic dispersion engineering of Rayleigh-type SAWs in SPnCs and the corresponding SAW transport under spatial lattice optimization. Theoretically, as such a material approaches a certain intrinsic geometrical lattice factor, the dispersion of Rayleigh-type SAWs will undergo a noticeable change, giving rise to an optimal flat dispersion ideal for slow SAW transport. We experimentally demonstrate that, in a material with this optimized configuration, the SAW speed can be dramatically reduced by a factor of 17.4, down to 200 m/s, a speed even slower than the speed of sound in air. Compared with the original unoptimized lattice, the optimized SPnC possesses a significantly broadened operation bandwidth, within which the SAW speeds are all less than 340 m/s. When applied to manipulate dispersion and generate slow waves, our technique enables the easy implementation of time-dependent modulation to realize advanced signal-processing functionalities, e.g., designable long-time acoustic delay lines and nonreciprocal acoustic transmission, and it may help to enhance the sensitivity of acoustic based sensors [53–59], acoustic nonlinear even quantum-dynamic interactions [60,61], and the control of microfluidics-based lab-on-a-chip systems [51,62]. Our findings may have broad implications for two-dimensional or quasi-two-dimensional wave systems (especially those localized on a surface) and semiconductor excitations using acoustic fields [63].

II. RESULTS AND DISCUSSION

A. Theoretical investigation of SAW dispersion with four basic SPnC configurations

Our chip-scale SPnCs are formed of solid pillars on a semi-infinite elastic substrate (see material details in Appendix A), through which planar SAWs pass, as shown in Fig. 1(a). To identify a nontrivial lattice configuration for these SPnCs that would be suitable for investigating the dispersion evolution, we initially consider four basic configurations, all with mirror symmetry about the SAW injection direction. They are, as shown in Figs. 1(b)–1(e), square-lattice SPnCs with the SAW injection direction aligned parallel to the Γ-X or Γ-M directions and triangular-lattice SPnCs with the SAW injection direction aligned parallel to the Γ-M or Γ-K direction, all with the same lattice constant a_0. The calculated band structures all contain a flat dispersion curve (solid gray) near the same normalized frequency of approximately 1670 Hz m, which corresponds to a LR mode, as shown in Fig. 2 The characteristics of this mode depend only on the material and geometrical properties of the solid pillars, which are the same in all four cases. Although this full-spectrum flat dispersion curve indicates a near-zero group velocity, this kind of mode is difficult to use in practice due to (1) weak coupling with incident Rayleigh waves and (2) the fact that any incident pulse must lie within a certain bandwidth; otherwise, smoothing or expansion of the pulse will occur [4]. In addition to the LR dispersion band, another dispersion band, labeled as S_0, also exists in all four configurations. The corresponding Bloch modes, shown in Fig. 2, clearly indicate that this dispersion band, S_0, originates from the substrate Rayleigh mode, and thus, these two corresponding modes efficiently couple with each other at the SPnC boundaries. The discussion that follows focuses primarily on this particular dispersion band.

In the first three configurations [Figs. 1(b)–1(d)], the S_0 dispersion possesses a positive but diminishing slope with an increasing Bloch momentum. Near the boundary of the first period along the SAW injection direction ($\vec{k}_x$) in reciprocal space (notably, although it is a two-dimensional lattice, the dispersion over one whole period in each direction should be investigated independently), the dispersion becomes very flat with a near-zero slope, thanks to the intense Bragg scattering at the Brillouin zone (BZ) boundary. In the fourth configuration [Fig. 1(e)], however, the S_0 dispersion band contains two subbranches, S_0+ and S_0-, each varying monotonically with the Bloch momentum but with opposite slopes. These subbranches are continuously differentiable at the boundary between them, i.e., the K point of the triangular lattice, where $|\vec{k}_x| = 4\pi/3a_0$. Hence, the S_0 dispersion curve exhibits two flat regions: one near the boundary of its first period ($|\vec{k}_x| = 2\pi/a_0$) and one

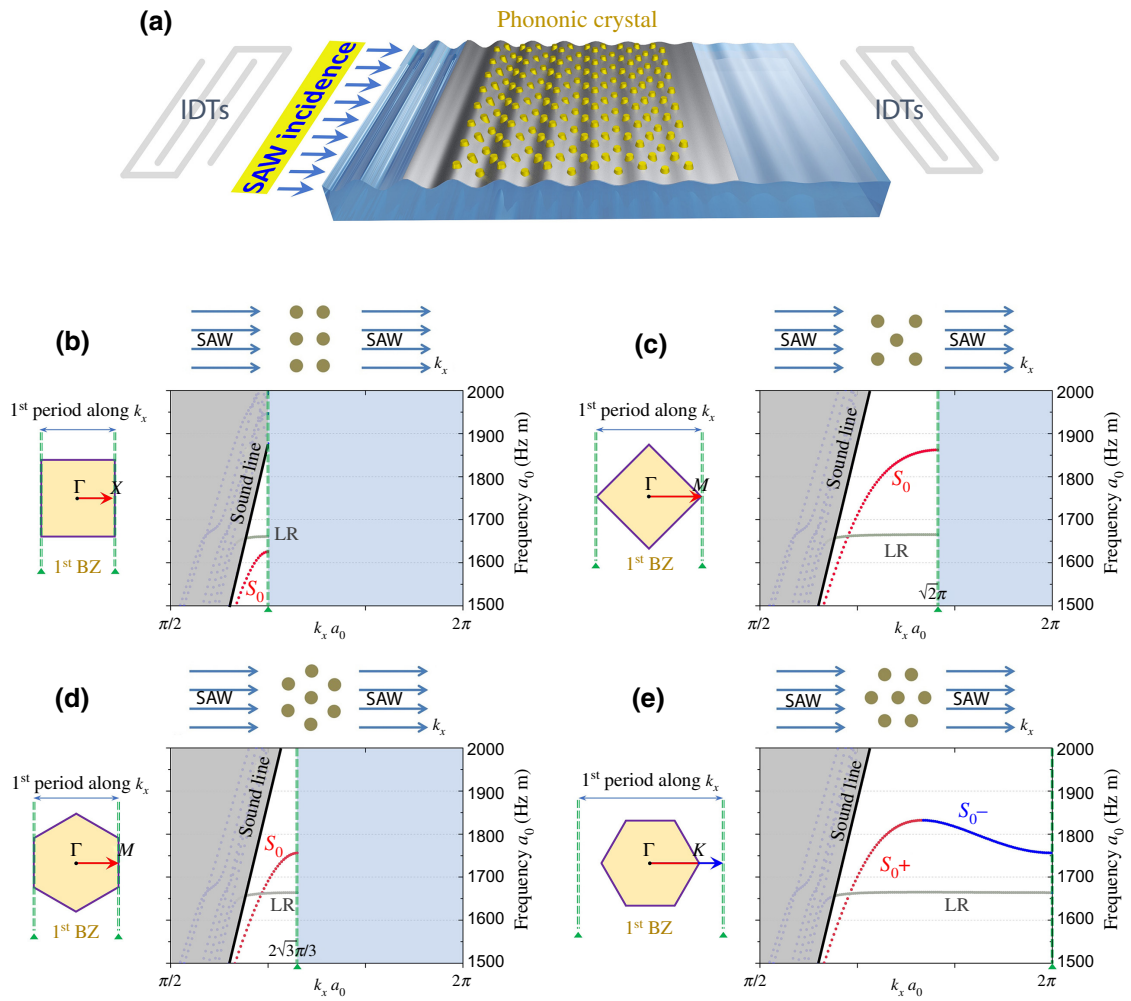

FIG. 1. SAW dispersion in four basic SPnC configurations and symmetries. This research is based on the platform shown in (a), namely, a chip-scale SPnC consisting of solid pillars on an elastic substrate, through which planar SAWs pass. Calculated band structures of the four considered cases of SAW incidence (along directions of high symmetry with respect to the SPnC) are shown: (b),(c) correspond to cases in which the SAWs are incident on a square-lattice SPnC in the Γ-X and Γ-M directions, respectively; (d),(e) correspond to cases in which the SAWs are incident on a triangular-lattice SPnC in the Γ-M and Γ-K directions, respectively. All surface modes lie below the sound line (black), which represents the slowest bulk acoustic modes. The flat dispersion curves (gray) near the frequency of 1670 Hz m are the localized resonant (LR) modes. S_0 dispersion bands are manifestations of the Rayleigh modes in the SPnCs.

near the region where the subbranches S_0+ and S_0- meet. These unique dispersion characteristics are very promising for the generation of broadband slow waves, since these two flat regions may start to merge as the lattice undergoes continuous variation, i.e., compression or stretching, along the direction perpendicular to the wave propagation direction $\vec{k_x}$.

B. Evolution of the SAW dispersion under lattice deformation

The theoretical deformation process of the triangular-lattice SPnC is schematically illustrated in Fig. 3(a). The original undeformed triangular lattice has a lattice constant of a_0, and b_0 denotes the distance between each unit cell and its next nearest neighbor in the y direction (i.e., $\sqrt{3}a_0$). During the deformation process (as the gray arrow indicates), spatial compression or stretching along the y direction changes only the spacing between two unit cells in the y direction, i.e., results in a separation distance of $b = rb_0$ (where r is the deformation ratio), while the thickness, L, of the SPnC and the unit cell spacing in the x direction remains unchanged. The corresponding surface acoustic dispersion relations in the x direction before and after the lattice deformation are illustrated in Figs. 3(b) and 3(c), respectively. Obviously, during the deformation process, since the geometric and elastic parameters of the solid pillars remain unchanged, the LR dispersion also remains

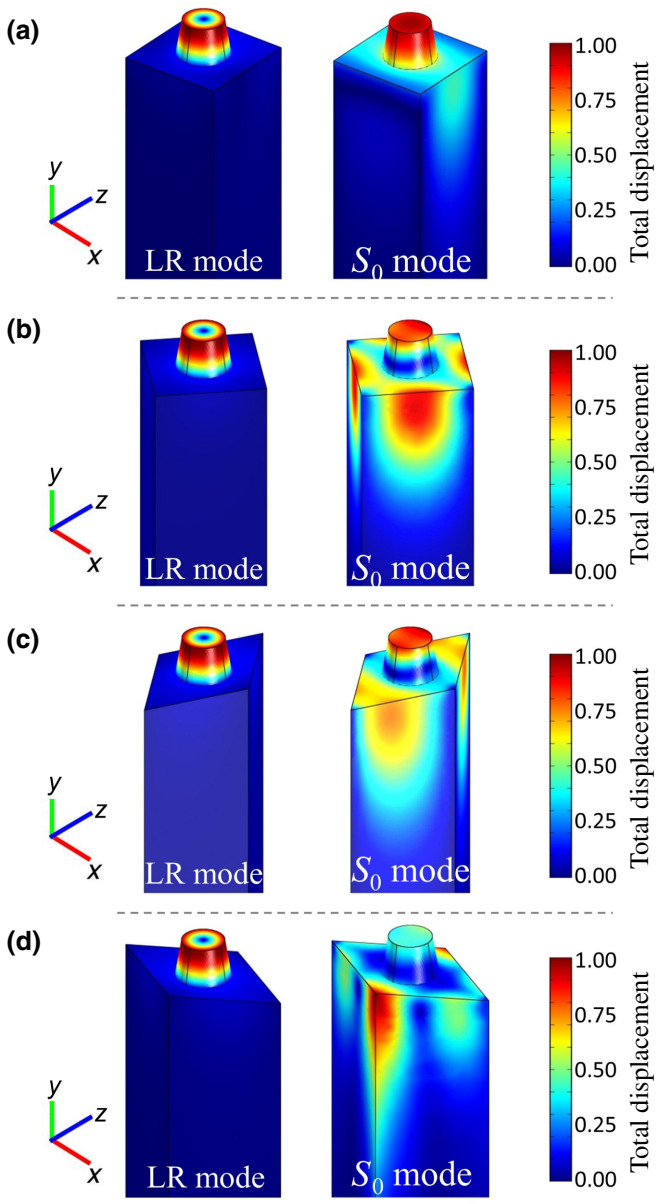

FIG. 2. Distributions of elastic fields in the modes and dispersion bands of the four different configurations. (a),(b) correspond to square-lattice SPnCs with SAWs incident along the Γ-X and Γ-M directions, respectively; (c),(d) correspond to triangular-lattice SPnCs with SAWs incident along the Γ-M and Γ-K directions, respectively.

unchanged near the normalized frequency of 1670 Hz m. The initially nonmonotonic S_0 dispersion, however, undergoes a dramatic change, as the deformation ratio r varies from 1.05 to 0.60. In particular, reducing the deformation ratio has the predominant overall effect of reducing the negative slope of the S_0- subbranch. Eventually, once a certain deformation ratio, r_t, is reached, this negative slope completely vanishes, and the S_0 dispersion transforms into a completely monotonic band with a positive slope.

Notably, r_t can be theoretically shown to exist in the deformation process of a two-dimensional triangular lattice by means of the tight-binding model (see Appendix B), but its value can vary from case to case, depending on the actual geometric and material elastic parameters of the solid pillars and substrate. We note that the theoretical findings agree well with finite element method (FEM) calculations (see Fig. 8 in Appendix B). These findings indicate that, during the lattice deformation process, a gradual change will occur in the coupling strength between nearest-neighbor pillars (except in the x direction). Specifically, when this coupling strength increases to nearly twice its original value, the S_0- subbranch (which initially has a negative dispersion slope) will merge into the S_0+ subbranch (the positive dispersion slope of which remains unchanged) to form a completely monotonic S_0 dispersion curve throughout the whole reciprocal region of $k_x a_0 \in [0, 2\pi]$. Unlike the traditional method of using strong scattering at the BZ boundaries to produce slow waves, our approach can, in principle, produce a slow-wave region that is no longer restricted to the BZ boundaries, thanks to the deformation-induced dispersion transition, potentially leading to a highly superior delay bandwidth for practical slow-wave applications [4].

C. Chip-scale experiment and device based on a $LiNbO_3$ substrate

The prototype SPnCs experimentally tested in this work are formed by electrochemically growing microscale nickel (Ni) pillars on a $LiNbO_3$ substrate. The fabricated pillars show a consistent cone-shaped geometry due to the thick resist used in the lithography step, as illustrated in Fig. 4(d). The elastic parameters of $LiNbO_3$ and the electroplated Ni pillars are taken from Refs. [64,65]. The piezoelectric module in the three-dimensional (3D) FEM using COMSOL Multiphysics is applied to calculated the band structures of our practical samples. An accurate diagram of the phase-change behavior as a function of the deformation ratio is calculated using these parameters and is shown in Fig. 4(a), where the red hexagons indicate the boundary in reciprocal space dividing the subbranches S_0+ and S_0-. Clearly, with the theoretical compression of the lattice, the boundary is pushed towards $k_x = 2\pi/a_0$. As a result, subbranch S_0- gradually merges with subbranch S_0+ and eventually completely vanishes beyond a certain phase-change point, which lies at a deformation ratio of $r_t \approx 0.80$ in this case.

A schematic of an on-chip signal delay line constructed with these slow-SAW structures is illustrated in Fig. 4(b); a corresponding photograph of a representative device during testing is shown in Fig. 4(c). A pair of identical broadband chirped electroacoustic transducers, one serving as a SAW generator and the other as a SAW receiver, are fabricated on the left and right sides of a piezoelectric $LiNbO_3$

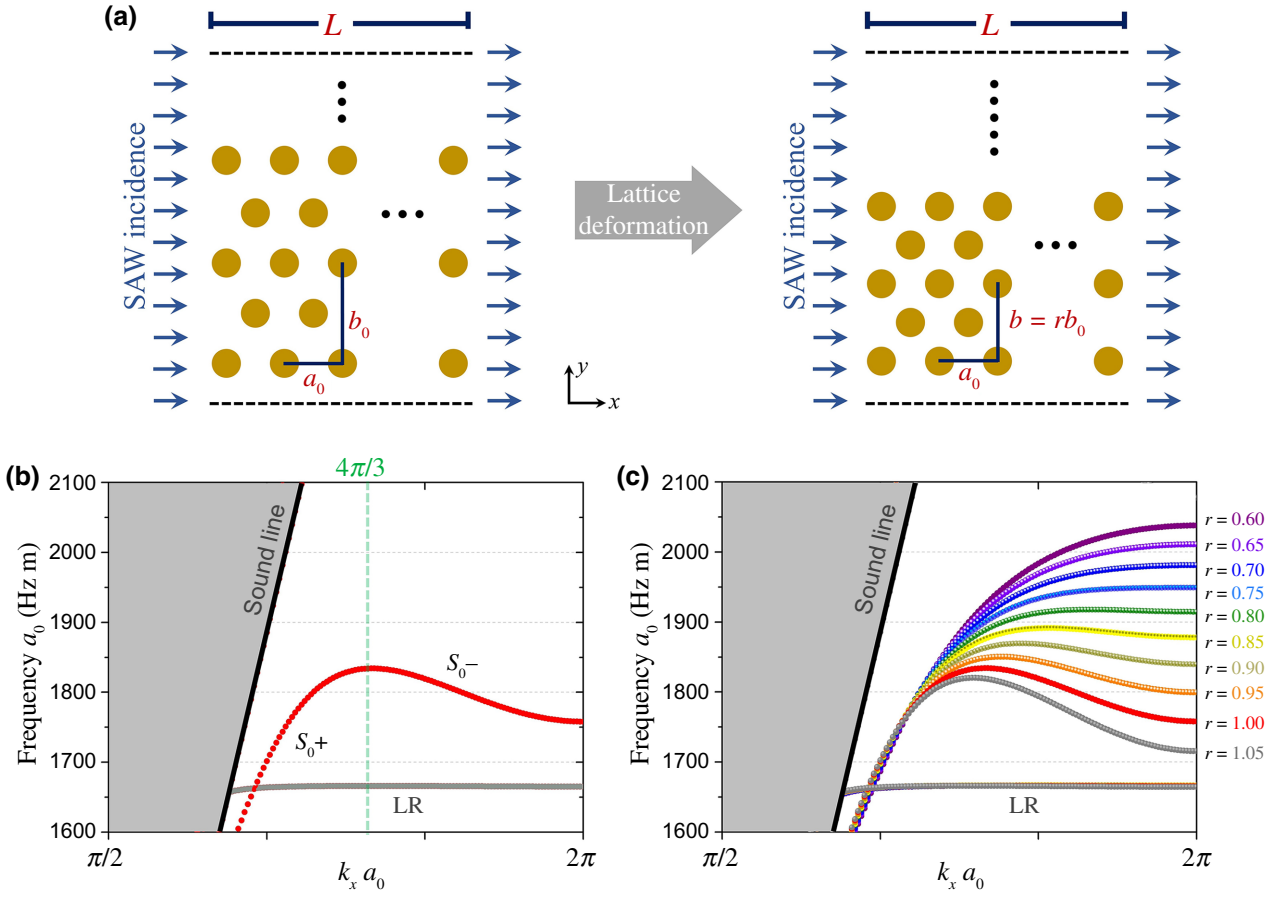

FIG. 3. Theoretical evolution of the SAW dispersion under lattice deformation. Deformation of the SPnC lattice is schematically illustrated in (a): in a triangular lattice of thickness L (left), the distance from each unit cell to its next-nearest neighbor in the x direction remains constant, while the distance in the y direction is evenly spatially compressed such that $b_0 \rightarrow b = rb_0$ (right). Corresponding band structures before and after the lattice deformation are illustrated in (b),(c), respectively. During the lattice deformation process, the initial S_0- dispersion curve (with a negative slope) is gradually integrated into S_0+ (with a positive slope) and eventually vanishes when r reaches a certain value (near 0.75). In this exact configuration, the now-unified dispersion band S_0 possesses the smallest but positive mean group velocity over the broadest frequency range, from the lower frequencies to the band edge.

substrate, which is chosen to be y-z cut to ensure better electromagnetic-to-acoustic coupling and lower SAW propagation loss in practice. These transducers have the same operation bandwidth, ranging from 66 to 86 MHz. By applying ac electrical power of this bandwidth to the left transducer, a Rayleigh-type SAW can be efficiently launched towards the right side to interact with the SPnCs.

D. Optimized slow SAWs with a broad operation bandwidth

Two different samples, one with an unoptimized triangular lattice to serve as a reference and the other with the optimized lattice corresponding to the phase-change point, are fabricated separately to study their SAW transmission characteristics. The corresponding scanning electron micrographs (SEMs) of these two samples are shown in Figs. 5(a) and 5(b), respectively. A vector network analyzer (Agilent 4396B) is used to acquire the amplitude response (transmission characteristics) and phase response (time delay) of our samples. All measurements are performed within the spectral window from 66 to 86 MHz in frequency increments of 100 kHz. The corresponding calculated band structures in the $\vec{k}_x$ direction of the two samples are shown in Figs. 5(c) and 5(d), respectively. The response of the pair of transducers responsible for generating and detecting SAWs is characterized in a back-to-back measurement (without any SPnCs on the substrate); the corresponding power transmission results are shown as black circles in Figs. 5(e) and 5(f), and the time delay results are shown as black diamonds in Figs. 5(g) and 5(h). It is clear that the response of our transducers is almost perfect, being nearly flat within the spectral range of interest. With the presence of the SPnCs on the substrate, a directional forbidden band in the $\vec{k}_x$ direction appears for both samples, as shown by data plotted as blue diamonds

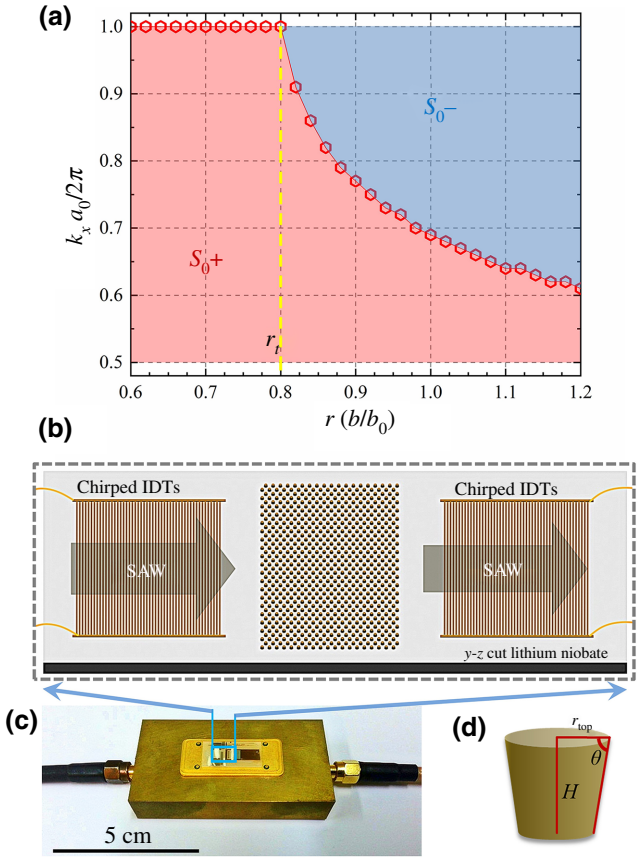

FIG. 4. Chip-scale experiment and device based on a $LiNbO_3$ substrate. For the materials used in our practical experiment, i.e., electroplated nickel (Ni) pillars on a $LiNbO_3$ substrate, the calculated diagram of the transformation of the S_0 dispersion during the theoretical lattice deformation process is illustrated in (a). Red hexagons indicate the boundary between S_0+ and S_0-. With compression of the lattice, dispersion subbranch S_0- is gradually integrated into S_0+ and eventually vanishes at $r_t = 0.80$, the phase-change point. Structure of a practical SPnC-based transmission line is schematically illustrated in (b). On y-z cut lithium niobate substrate, a broadband SAW ranging from 66 to 86 MHz is generated from one electroacoustic transducer; transmitted through the SPnC, in which the SAWs are slowed; and eventually received in the crystallographic z direction. Real device, prepared with practical SPnCs composed of electroplated nickel pillars attached to the substrate, is shown in (c); these pillars all have the same geometry, which is shown in (d). Typical sidewall angle θ for these pillars is approximately 84° (limited by the sample-processing technology). Top radius r_{top} and height H of the pillars are measured to be 6.0 and 7.4 μm, respectively.

in Figs. 5(e) and 5(f). The band edge lies at 73.6 MHz for the reference sample with the unoptimized lattice, while it is blueshifted to 78.8 MHz for the lattice-optimized sample. Notably, these two values match well with our FEM calculation results, as indicated by the shaded regions in the plots. The time-delay spectra, shown as blue diamonds in Figs. 5(g) and 5(h) for both samples, reveal an increase in the delay time as the frequency approaches the edge of the forbidden band. However, the time delay for the lattice-optimized sample near the band edge is almost twice that for the unoptimized reference sample, and the bandwidth for a given time-delay value, e.g., 0.9 μs, for the lattice-optimized sample is much larger than that for the reference sample. These findings suggest that our approach of delaying SAWs by means of an optimized lattice is indeed effective and advantageous compared with the exploitation of strong Bragg scattering at the BZ boundary.

The additional time delay observed in these SPnCs can be correlated with the group delay of the SAWs, which can be characterized by the group indexes $n_g \equiv v_o/v_g$ of the two samples, where $v_0 = 3488$ m/s is the velocity of Rayleigh-type SAWs in the y-z cut $LiNbO_3$ substrate (which is invariant within the frequency range of interest) and v_g is the group velocity of the SAWs in the SPnCs. n_g can be experimentally estimated from the measured time-delay spectra as $n_g = (t - t_0)v_0/L + 1$, considering that the Rayleigh mode does not experience any dispersion in the frequency range of interest, where t and t_0 are the time delays with and without the SPnCs, respectively. In addition, n_g can also be deduced directly from the numerically calculated dispersion relation, in accordance with its definition, $n_g = v_0(dk/d\omega)$, where k is the Bloch momentum and ω is the angular frequency. The corresponding results are plotted in Figs. 5(i) and 5(j). Experimental data will be considered in the following discussion. First, our experimental results agree very well with theory. For the lattice-optimized sample, an extra-large measured group-index value of 17.4 occurs at the frequency of 78.4 MHz, which is close to but not within the forbidden band; thus, considerable SAW transmittance is still maintained. This finding means that the velocity of the elastic SAWs is slowed to 1/17.4 of the value for the plain substrate, reaching a remarkably low speed of 200 m/s, which is even slower than the speed of sonic waves in air, i.e., 340 m/s. Moreover, compared with the unoptimized reference SPnC sample with the original triangular lattice, the lattice-optimized SPnC sample possesses a significantly broader operation frequency range (with a bandwidth of approximately 1.4 MHz), in which the velocities of the slow SAWs are all less than 340 m/s, as indicted by the yellow highlighted region in Fig. 5(j).

E. Dynamic transduction and delay of signals in wave packets

After demonstrating the transmittance properties of the SPnCs for slow SAWs, we further verify their dynamic transduction properties for signals with arbitrary waveforms. Several deliberately designed SAW Gaussian pulses with identical bandwidths of 1 MHz, but different center frequencies f_c, are experimentally injected into the lattice-optimized sample [depicted in Fig. 5(b)], and the

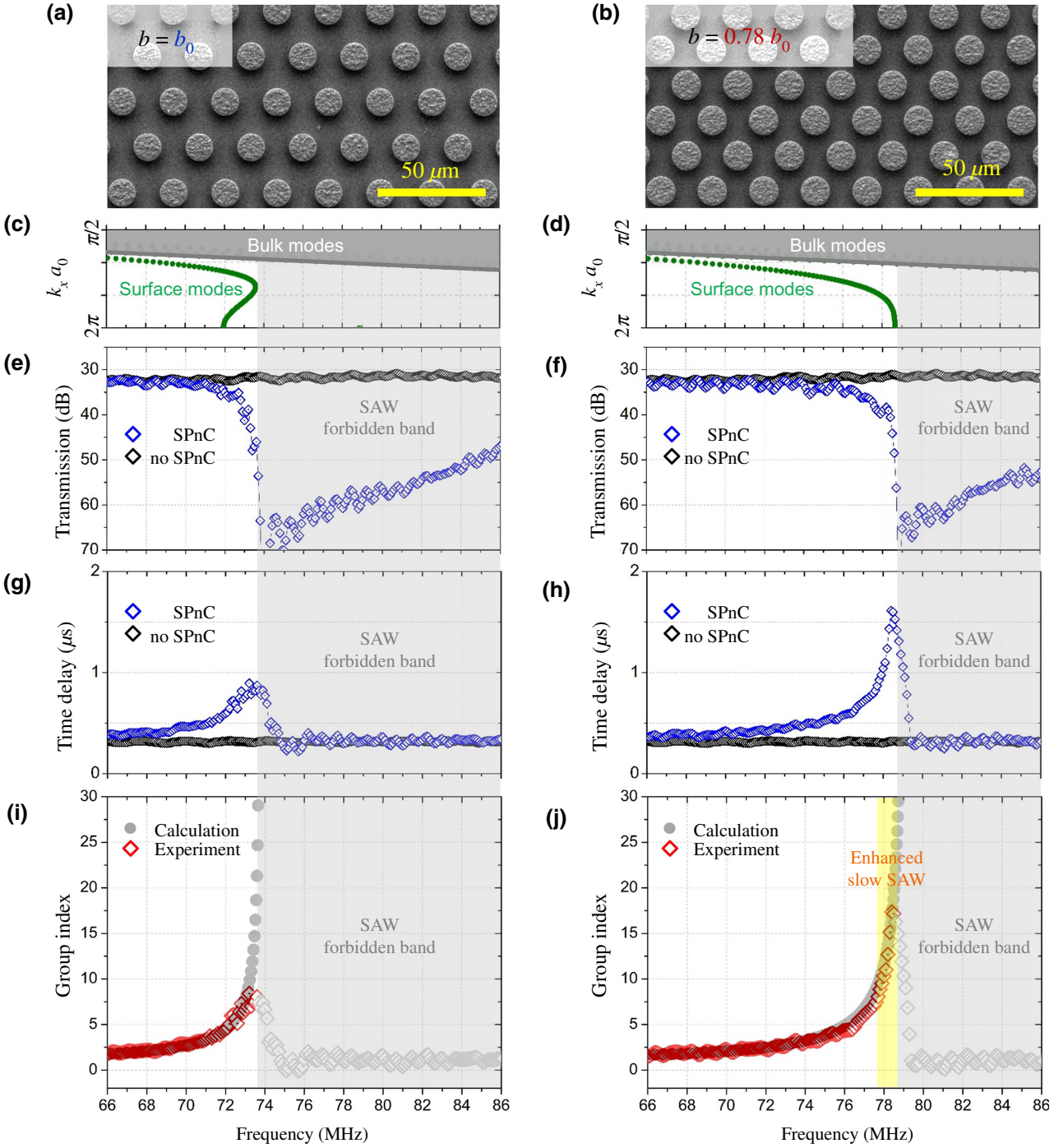

FIG. 5. Optimized slow SAWs with a broad operation bandwidth. Comparative experiments are conducted using one reference sample with the original triangular lattice ($b = b_0$) and one lattice-optimized sample ($b = 0.78b_0$), slightly over the point of total transition ($r_t b_0 = 0.80b_0$). The corresponding results are shown in (a),(c),(e),(g),(h) and (b),(d),(f),(h),(j), respectively. (a),(b) present SEMs of the SPnCs. (c),(d) present the calculated band structures along k_x (Γ-K direction). Transmittance spectra in (e),(f) confirm that SAW-forbidden bands (gray) start at 73.6 and 78.8 MHz, respectively. In (g),(h), time-delay spectra of the whole transmission line are plotted. Group-index spectra are plotted in (i),(j), indicating the extent of SAW slowdown. In the lattice-optimized sample, SAWs are slowed down to a greater extent and over a much broader range, from frequencies of higher than 77.6 MHz to the forbidden band, as indicated by the yellow highlighted region. Ultraslow SAW is measured at 78.4 MHz, near the forbidden band but still with an appreciable transmittance (> -10 dB); its velocity reaches 200 m/s, even slower than the speed of sound in air.

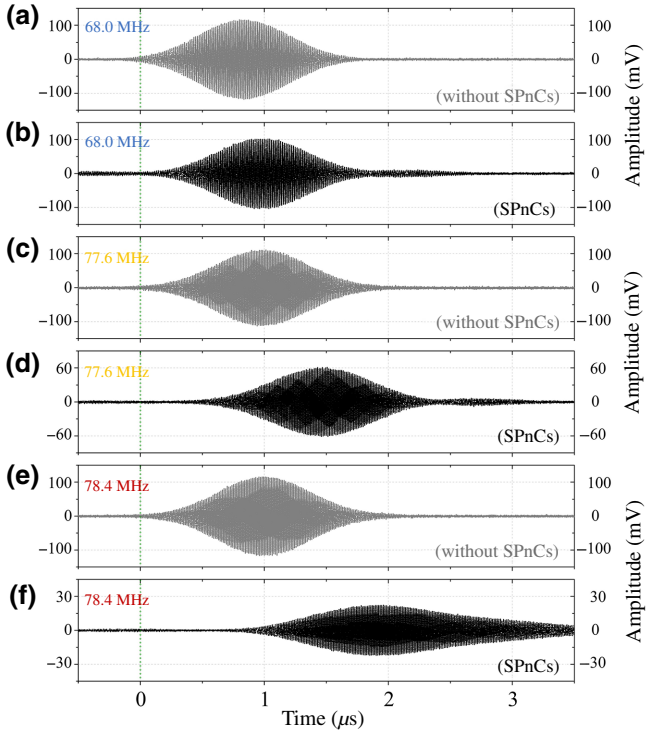

FIG. 6. Dynamic transduction or delay of signals in wave packets. SAW Gaussian pulses with identical bandwidths (1 MHz) and different center frequencies, f_c, are injected into the lattice-optimized sample depicted in Fig. 5(b), and corresponding time-dependent transmission spectra are shown. (a),(b) correspond to the case of $f_c = 68$ MHz; (c),(d) correspond to the case of $f_c = 77.6$ MHz; (e),(f) correspond to the case of $f_c = 78.4$ MHz. Spectra presented in (a),(c),(e) serve as references, representing the scenario without any SPnCs placed in the transmission and time-delay line; here, amplitudes of the transmitted electrical signals reach approximately 115 mV. Net time delays in these three cases are measured to be 0.13, 0.48, and 0.89 μs, respectively. All cases exhibit near-perfect properties of signal restoration and still-appreciable transmittance, with measured amplitudes of approximately 100, 50, and 30 mV, respectively.

time-dependent transmission spectra are measured, with the results presented in Fig. 6.

Figures 6(a) and 6(b) correspond to cases with f_c equal to 68.0 MHz, Figs. 6(c) and 6(d) correspond to cases with f_c equal to 77.6 MHz, and Figs. 6(e) and 6(f) correspond to cases with f_c equal to 78.4 MHz. The results shown in Figs. 6(a), 6(c), and 6(e) act as references, representing the scenario without any SPnCs placed in the transmission line; in these cases, the amplitudes of the transmitted electrical signals reach the same value of nearly 115 mV. The electrical time delays of the received Gaussian pulses in these three cases are measured to be 0.13, 0.48, and 0.89 μs, respectively, which are consistent with the theoretically calculated values. At 77.6 MHz, the features of the transmitted Gaussian pulse are perfectly restored after passing through the time-delay line, and a considerable amplitude of 50 mV is maintained. In contrast, at 78.4 MHz, since this frequency is very close to the SAW forbidden band, the bandwidth of the transmitted signal is somewhat reduced; hence, the waveform of the restored Gaussian pulse is slightly broadened, although its amplitude is still appreciable, with a value of 30 mV.

III. CONCLUSION

We propose an effective method of engineering a designable shallow dispersion band structure in a tight-binding-type two-dimensional periodic medium. Theoretically, when a wave is propagating along the Γ-K direction in a conventional triangular lattice, if the lattice is spatially compressed in the direction perpendicular to wave propagation, then the negative slope of the initial dispersion subbranch S_0- in reciprocal space will gradually diminish. In the exact configuration in which the S_0- dispersion eventually vanishes, a flat dispersion curve that is promising for the creation of ideal slow-wave devices is achieved. Whether for electrons, photons, or phonons, this method can give rise to dispersions with ultrasmall but positive values (group velocities) over a relatively broad operation bandwidth. In a comparative experiment, on-chip SAW transmission lines integrated with microscale SPnCs composed of elaborate nickel pillars attached to a $LiNbO_3$ substrate are fabricated. In the lattice-optimized sample, with a compression ratio of 0.80, an ultraslow SAW transmission is measured at a frequency of 78.4 MHz, showing a remarkable ultraslow surface elastic velocity below even the speed of sound in air. More importantly, compared with the unoptimized reference sample with the original triangular lattice, the lattice-optimized sample possesses a significantly broader operation bandwidth of approximately 1.4 MHz, in which the SAW velocities are all less than 340 m/s. Our approach lays the foundation for versatile delay lines that can achieve signal restoration with relatively low energy consumption. Additionally, for surface wave devices, our approach offers the possibility of real-time tunability, if a flexible or stretchable substrate were to be introduced [66]. Furthermore, such man-made ultraslow waves are excellent candidates for use in time- and phase-varying devices and high-sensitivity detectors in the fields of telecommunication and medical, biological, and environmental research.

ACKNOWLEDGMENTS

The work is jointly supported by the National Key R&D Program of China (Grants No. 2017YFA0305100, No. 2017YFA0303702, and No. 2018YFA0306200), the National Natural Science Foundation of China (Grants No. 51702152, No. 11874196, No. 11625418, No. 11890702, and No. 51721001). We also acknowledge the support of the Natural Science Foundation of Jiangsu Province

and support from the Academic Program Development of Jiangsu Higher Education (PAPD). J.C. acknowledges support from the European Research Council (ERC) through Starting Grant No. 714577 PHONOMETA and from the MINECO through a Ramón y Cajal grant (Grant No. RYC-2015-17156).

APPENDIX A: SURFACE ACOUSTIC BAND STRUCTURES OF FOUR BASIC SPnC CONFIGURATIONS

In the initial design phase, we consider the practical cases of Rayleigh-type SAWs stimulated by IDTs and normally incident on an SPnC (in which the SAWs are slowed down). Because the incident SAWs should experience no deflections in the SPnC, their direction of incidence or propagation should be parallel to one of the most highly symmetric orientations of the SPnC. Put simply, the orientation of the two-dimensional SPnC should exhibit mirror symmetry with respect to the incident waves. Consequently, we consider the four basic configurations illustrated in Fig. 1 of the main text. Figures 1(b) and 1(c) correspond to the cases of SAWs incident on square-lattice SPnCs in the Γ-X and Γ-M directions, respectively; Figs. 1(d) and 1(e) correspond to the cases of SAWs incident on triangular-lattice SPnCs in the Γ-M and Γ-K directions, respectively.

The corresponding surface acoustic band structures in the wave propagation direction ($\vec{k_x}$) are calculated via 3D FEM using COMSOL Multiphysics, and the results are illustrated in Fig. 1 below the configuration schematics. All surface acoustic modes lie below the solid black sound line in each plot, which represents the slowest bulk dispersion, corresponding to the boundary between the bulk and surface modes. In the 3D FEM calculations, both the square- and triangular-lattice SPnCs have the same lattice constant (equal to the normalized value $r_{\text{square}} = r_{\text{triangular}} = 1$ m) and are made of identical metal pillars with the same elastic and geometric properties (with a mass density, Young's modulus, and Poisson's ratio equal to 8906 kg/m^3, 1.1×10^{11} Pa, and 0.31, respectively, and with a top radius r_{top} and height H equal to 0.22 and 0.35 m, respectively) attached to a theoretically isotropic elastic substrate (with a mass density, Young's modulus, and Poisson's ratio of 4650 kg/m^3, 2.0×10^{11} Pa, and 0.33, respectively.).

In all of these cases, an identical flat (solid gray) dispersion curve appears at a frequency of approximately 1670 Hz m. This dispersion experiences barely any spatial influence, except near the sound line; in fact, it corresponds to a LR mode (as illustrated in Fig. 2) with characteristics determined only by the pillar parameters, with little relation to the bottom substrate and lattice symmetry. This LR mode has a near-zero group velocity throughout the whole spectrum and weak conversion efficiency with respect to the incident Rayleigh waves.

In addition to the LR dispersion band, another distinct dispersion band appears in each of these four cases. From an examination of the elastic field distributions of the modes in these dispersion bands (as illustrated in Fig. 2), it is clear that all of these modes possess similar symmetric features with respect to the propagation direction (thus, we name them S_0 modes or dispersion bands), and their energies are mostly confined within 1–2 wavelengths of the substrate surface. These modes are actually manifestations of the Rayleigh modes in the SPnCs; incident Rayleigh waves can be spontaneously converted into these modes at the SPnC boundaries, and thus, these modes are of high value for practical applications.

In the cases depicted in Figs. 1(b)–1(d), the S_0 dispersion bands exhibit consistent monotonicity, with a positive slope throughout the entire Bloch momentum range. Near the boundaries of the first period along the $\vec{k_x}$ direction, because of intense Bragg scattering, these dispersion curves are flattened, with their dispersion values rapidly approaching zero. However, in the case depicted in Fig. 1(e), the S_0 dispersion band exhibits entirely different features. This dispersion curve is not monotonic throughout the entire Bloch momentum range; instead, it consists of two independently monotonic subbranches, S_0+ (red) and S_0- (blue), as labeled in Fig. 1. These subbranches are both monotonic, with opposite slopes. They are continuously differentiable at the boundary between them, at $|\vec{k_x}| = 4\pi/3a$ (the highly symmetric K point in a standard triangular lattice). Therefore, overall, the corresponding dispersion curve in Fig. 1(e) is flattened not only at its band edge, where $|\vec{k_x}| = 2\pi/a_0$, but also at the boundary between S_0+ and S_0-.

APPENDIX B: TIGHT-BINDING THEORY OF LATTICE DEFORMATION

After lattice deformation, as illustrated in Fig. 7, the basis vectors in real space are

$$\vec{a}_1 = \frac{a}{2}\hat{e}_x - \frac{b}{2}\hat{e}_y,$$
$$\vec{a}_2 = \frac{a}{2}\hat{e}_x + \frac{b}{2}\hat{e}_y. \tag{B1}$$

a and b are the distances between nearest-neighbor unit cells. Let $\beta = b/a$, then, the basis vectors change to

$$\vec{a}_1 = \frac{a}{2}(\hat{e}_x - \beta\hat{e}_y),$$
$$\vec{a}_2 = \frac{a}{2}(\hat{e}_x + \beta\hat{e}_y). \tag{B2}$$

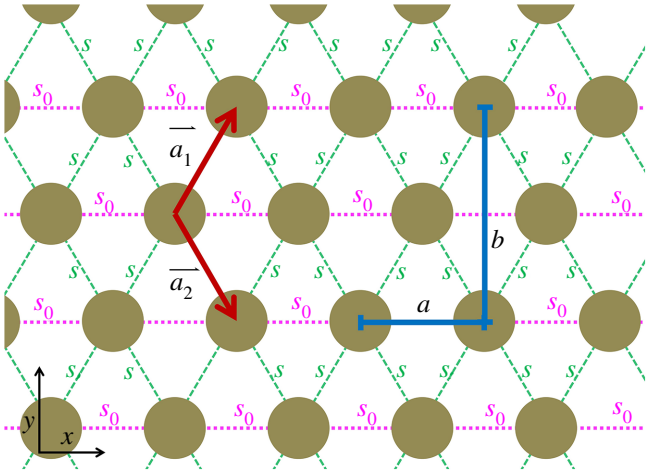

FIG. 7. Tight-binding model of lattice deformation. $\vec{a}_1$ and $\vec{a}_2$ are the basis vectors in real space. a and b are the distances between nearest-neighbor unit cells in the x and y directions, respectively. s_0 and s are the coupling strengths between pillars in the x direction and diagonal direction, respectively.

These basis vectors in reciprocal space are

$$\vec{b}_1 = \frac{2\pi}{\Omega}(\vec{a}_2 \times \hat{e}_z) = \frac{2\pi}{a}\left(\vec{e}_x - \frac{1}{\beta}\vec{e}_y\right),$$
$$\vec{b}_2 = \frac{2\pi}{\Omega}(\hat{e}_z \times \vec{a}_1) = \frac{2\pi}{a}\left(\vec{e}_x + \frac{1}{\beta}\vec{e}_y\right). \tag{B3}$$

Then, the boundary point of the first BZ in the $\vec{k}_x$ direction can be calculated as

$$k = \left[\left(\frac{1}{2} + \frac{1}{2\beta^2}\right)\frac{2\pi}{a}, 0\right]. \tag{B4}$$

With the spatial deformation of the SPnC, the S_0- dispersion finally disappears at

$$k = (2\pi/a, 0). \tag{B5}$$

The distance in the $\vec{k}_x$ direction between Eqs. (B4) and (B5) is

$$\left(\frac{1}{2} + \frac{1}{2\beta^2}\right)\frac{2\pi}{a} - \frac{2\pi}{a} = \frac{1-\beta^2}{2\beta^2}\frac{2\pi}{a}. \tag{B6}$$

During the spatial deformation process, as shown in Fig. 2, the value of β is always larger than one (when $b = 0.60b_0$, $\beta = 0.6\sqrt{3} \approx 1.039$); therefore, the value of Eq. (B6) is always larger than zero. Thus, it is clear that, except in the case of the nondeformed standard triangular lattice when $\beta = \sqrt{3}$, the boundary between the dispersion subbranches S_0+ and S_0- is not the boundary of the first BZ.

According to tight-binding band theory, when there is only one wave function in the unit cell, the approximate formula for the dispersion is

$$E(\vec{k}) = E_n - J(0) - \sum_{R_s \neq 0}^{\text{nearest-neighbors}} J(\vec{R}_s)e^{-i\vec{k}\cdot\vec{R}_s}, \tag{B7}$$

where $E_n - J(0)$ can be regarded as zero energy and $\vec{R}_s$ is the vector difference between lattice points.

In the first-order tight-binding approximation, we consider only the couplings between nearest-neighbor pillars in the SPnC, i.e., s_0 and s, as illustrated in Fig. 7. Thus, when only the nearest-neighbor terms in Eq. (B7) are preserved, the dispersion changes to

$$\begin{aligned} E(\vec{k}) &= -s_0 \sum_{\pm(\vec{a}_1+\vec{a}_2)} e^{-i\vec{k}\cdot\vec{R}_s} - s \sum_{\pm\vec{a}_1,\pm\vec{a}_2} e^{-i\vec{k}\cdot\vec{R}_s} \\ &= -2s_0\left[\cos(k_x a) + \mu\cos\left(\frac{k_x a}{2} + \frac{k_y a\beta}{2}\right)\right. \\ &\quad \left. + \mu\cos\left(-\frac{k_x a}{2} + \frac{k_y a\beta}{2}\right)\right], \end{aligned} \tag{B8}$$

where $\mu = s/s_0$. Since we consider only the dispersion in the direction of $\vec{k}_x$, $k_y = 0$, Eq. (B8) can be simplified to

$$E(k_x) = -2s_0\left[\cos(k_x a) + 2\mu\cos\left(\frac{k_x a}{2}\right)\right]. \tag{B9}$$

At the inflection points, we have

$$\frac{\partial E}{\partial k_x} = 0. \tag{B10}$$

By combining Eq. (B10) with Eq. (B9), we find that the inflection points should satisfy

$$\begin{aligned} \sin(k_x a) + \mu\sin\left(\frac{k_x a}{2}\right) &= \sin\left(\frac{k_x a}{2}\right) \\ &\quad \times\left[2\cos\left(\frac{k_x a}{2}\right) + \mu\right] = 0. \end{aligned} \tag{B11}$$

There are three inflection points in the region of $(k_x a/2) \in [0, \pi]$:

$$\begin{aligned} k_x &= 0, \\ k_x &= \frac{2\pi}{a}, \\ \cos\left(\frac{k_x a}{2}\right) &= -\frac{\mu}{2}. \end{aligned} \tag{B12}$$

To assess the convexity-concavity of these inflection points, we calculate the second-order derivative of

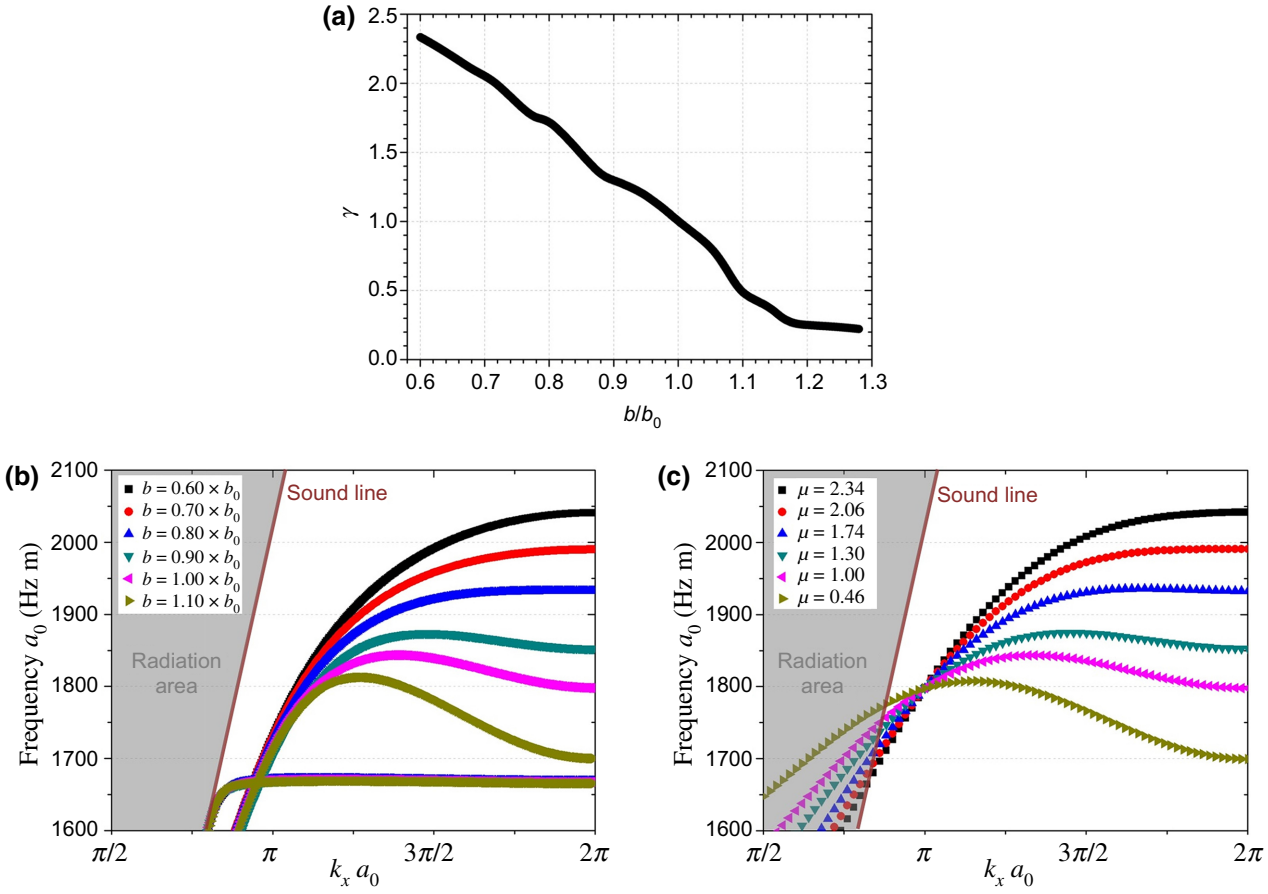

FIG. 8. Results of the tight-binding analysis. (a) Relationship between the coupling strength and spatial compression ratio. (b),(c) Band structures according to 3D FEM calculations and two-dimensional tight-binding theory, respectively.

Eq. (B9),

$$\frac{\partial^2 E}{\partial k_x^2} = 2s_0a^2\left(\cos(k_xa) + \frac{\mu}{2}\cos\left(\frac{k_xa}{2}\right)\right)$$
$$= \begin{cases} 2s_0a^2\left(1+\frac{\mu}{2}\right), k_x = 0, \\ 2s_0a^2\left(1-\frac{\mu}{2}\right), k_x = \frac{2\pi}{a}, \\ 2s_0a^2\left(1-\frac{\mu^2}{4}\right), \cos\left(\frac{k_xa}{2}\right) = -\frac{\mu}{2}, \end{cases} \tag{B13}$$

Then, we can analyze the situation by considering the value of μ in Eq. (B13)

(1) If $\mu < 2$, there are three inflection points:

$$k_x = 0,$$
$$k_x = \frac{2\pi}{a}, \frac{\partial^2 E}{\partial k_x^2} > 0, \tag{B14}$$
$$\cos\left(\frac{k_xa}{2}\right) = -\frac{\mu}{2}, \frac{\partial^2 E}{\partial k_x^2} < 0, \tag{B15}$$

(2) If $\mu \geq 2$, there are two inflection points:

$$k_x = 0,$$
$$k_x = \frac{2\pi}{a}, \frac{\partial^2 E}{\partial k_x^2} < 0. \tag{B16}$$

From the above, it can be seen that, during the lattice deformation process (along the y direction of the SPnC), the coupling strength between nearest-neighbor pillars will change. When the coupling strength between nearest-neighbor pillars in the diagonal direction (not along the x direction) changes to twice its original value, i.e., when $\mu = 2$, in the region of $(k_xa/2) \in [0, \pi]$, the S_0- subbranch (initially with a negative slope) will be totally integrated into the S_0+ subbranch (with a positive slope). We refer to this configuration as the point of total transition in the spatial compression of the (original) triangular lattice.

By comparing the results of tight-binding theory with those of the 3D FEM calculations, the relationship between the coupling strength and spatial compression ratio can be fitted, as plotted in Fig. 8(a). The following overall

conclusions can be drawn: during the compression process ($b/b_0 < 1.0$), the coupling strength between nearest-neighbor pillars in the diagonal direction (not along the x direction) increases approximately linearly; during the stretching process ($b/b_0 > 1.0$), the coupling strength between nearest-neighbor pillars in the diagonal direction decreases monotonically, but the decreasing trend slows down when $b/b_0 > 1.1$.

Figures 8(b) and 8(c) show the band structures obtained from the 3D FEM calculations and tight-binding theory, respectively. Because the two-dimensional tight-binding model cannot capture the dimension normal to the surface of the SPnC, the band structures shown in Fig. 8(c) do not reflect the distinction between bulk acoustic waves and SAWs, meaning that no sound line exists here. For ease of comparison, however, we still indicate the sound line and the radiation area [which are the same as those in Fig. 8(b)] in Fig. 8(c). It is clear that, near the radiation area (for small wave vectors), the results of the tight-binding method are not consistent with the 3D FEM results. However, far from the radiation area, especially for wave vectors close to the band edge at $|\vec{k}_x| = 2\pi/a$, the results of the tight-binding method agree well with those of the 3D FEM—during the lattice deformation process, the diminishment of S_0- can be clearly observed in both sets of results.

[1] M. S. Bigelow, N. N. Lepeshkin, and R. W. Boyd, Superluminal and slow light propagation in a room-temperature solid, Science **301**, 200 (2003).

[2] Y. Okawachi, M. S. Bigelow, J. E. Sharping, Z. Zhu, A. Schweinsberg, D. J. Gauthier, R. W. Boyd, and A. L. Gaeta, Tunable all-Optical Delays via Brillouin Slow Light in an Optical Fiber, Phys. Rev. Lett. **94**, 153902 (2005).

[3] Y. A. Vlasov, M. O'boyle, H. F. Hamann, and S. J. McNab, Active control of slow light on a chip with photonic crystal waveguides, Nature **438**, 65 (2005).

[4] T. Baba, Slow light in photonic crystals, Nat. Photonics **2**, 465 (2008).

[5] S. Residori, U. Bortolozzo, and J. Huignard, Slow and Fast Light in Liquid Crystal Light Valves, Phys. Rev. Lett. **100**, 203603 (2008).

[6] Q. Gan, Z. Fu, Y. J. Ding, and F. J. Bartoli, Ultrawide-bandwidth Slow-Light System Based on THz Plasmonic Graded Metallic Grating Structures, Phys. Rev. Lett. **100**, 256803 (2008).

[7] A. H. Safavi-Naeini, T. M. Alegre, J. Chan, M. Eichenfield, M. Winger, Q. Lin, J. T. Hill, D. E. Chang, and O. Painter, Electromagnetically induced transparency and slow light with optomechanics, Nature **472**, 69 (2011).

[8] B. Wu, J. F. Hulbert, E. J. Lunt, K. Hurd, A. R. Hawkins, and H. Schmidt, Slow light on a chip via atomic quantum state control, Nat. Photonics **4**, 776 (2010).

[9] A. Santillán and S. I. Bozhevolnyi, Demonstration of slow sound propagation and acoustic transparency with a series of detuned resonators, Phys. Rev. B **89**, 184301 (2014).

[10] G. Theocharis, O. Richoux, V. R. García, A. Merkel, and V. Tournat, Limits of slow sound propagation and transparency in lossy, locally resonant periodic structures, New J. Phys. **16**, 093017 (2014).

[11] C.-Y. Sun, J.-C. Hsu, and T.-T. Wu, Resonant slow modes in phononic crystal plates with periodic membranes, Appl. Phys. Lett. **97**, 031902 (2010).

[12] J. Zhu, Y. Chen, X. Zhu, F. J. Garcia-Vidal, X. Yin, W. Zhang, and X. Zhang, Acoustic rainbow trapping, Sci. Rep. **3**, 1728 (2013).

[13] X. Zhu, K. Li, P. Zhang, J. Zhu, J. Zhang, C. Tian, and S. Liu, Implementation of dispersion-free slow acoustic wave propagation and phase engineering with helical-structured metamaterials, Nat. Commun. **7**, 11731 (2016).

[14] C. J. Chang-Hasnain, P.-C. Ku, J. Kim, and S.-L. Chuang, Variable optical buffer using slow light in semiconductor nanostructures, Proc. IEEE **91**, 1884 (2003).

[15] R. S. Tucker, P.-C. Ku, and C. J. Chang-Hasnain, Slow-light optical buffers: Capabilities and fundamental limitations, J. Lightwave Technol. **23**, 4046 (2005).

[16] R. M. Camacho, C. J. Broadbent, I. Ali-Khan, and J. C. Howell, All-optical Delay of Images Using Slow Light, Phys. Rev. Lett. **98**, 043902 (2007).

[17] L. Thévenaz, Slow and fast light in optical fibres, Nat. Photonics **2**, 474 (2008).

[18] B. Wang, M. A. Dündar, R. Nötzel, F. Karouta, and S. He, And R. W. van der heijden, photonic crystal slot nanobeam slow light waveguides for refractive index sensing, Appl. Phys. Lett. **97**, 151105 (2010).

[19] H. Zhang, M. Sabooni, L. Rippe, C. Kim, S. Kröll, L. V. Wang, and P. R. Hemmer, Slow light for deep tissue imaging with ultrasound modulation, Appl. Phys. Lett. **100**, 131102 (2012).

[20] B. Corcoran, C. Monat, C. Grillet, D. J. Moss, B. J. Eggleton, T. P. White, L. O'Faolain, and T. F. Krauss, Green light emission in silicon through slow-light enhanced third-harmonic generation in photonic-crystal waveguides, Nat. Photonics **3**, 206 (2009).

[21] M. Bajcsy, S. Hofferberth, V. Balic, T. Peyronel, M. Hafezi, A. S. Zibrov, V. Vuletic, and M. D. Lukin, Efficient all-Optical Switching Using Slow Light Within a Hollow Fiber, Phys. Rev. Lett. **102**, 203902 (2009).

[22] P. Siddons, N. C. Bell, Y. Cai, C. S. Adams, and I. G. Hughes, A gigahertz-bandwidth atomic probe based on the slow-light Faraday effect, Nat. Photonics **3**, 225 (2009).

[23] C. Monat, M. De Sterke, and B. Eggleton, Slow light enhanced nonlinear optics in periodic structures, J. Opt. **12**, 104003 (2010).

[24] C. Kittel and P. McEuen, *Introduction to Solid State Physics* (Wiley, New York, 1976).

[25] E. Yablonovitch, Photonic band-gap structures, J. Opt. Soc. Am. B **10**, 283 (1993).

[26] J. Joannopoulos, R. Meade, and J. Winn, *Photonic Crystals* (Princeton Univ. Press, Princeton, NJ, 1995).

[27] J. Foresi, P. R. Villeneuve, J. Ferrera, E. Thoen, G. Steinmeyer, S. Fan, J. Joannopoulos, L. Kimerling, H. I. Smith, and E. Ippen, Photonic band gap microcavities in optical waveguides, Nature **390**, 143 (1997).

[28] M. S. Kushwaha, P. Halevi, L. Dobrzynski, and B. Djafari-Rouhani, Acoustic Band Structure of Periodic Elastic Composite, Phys. Rev. Lett. **71**, 2022 (1993).

[29] Z. Liu, X. Zhang, Y. Mao, Y. Zhu, Z. Yang, C. T. Chan, and P. Sheng, Locally resonant sonic materials, Science **289**, 1734 (2000).

[30] X.-F. Li, X. Ni, L. Feng, M.-H. Lu, C. He, and Y.-F. Chen, Tunable Unidirectional Sound Propagation Through a Sonic-Crystal-Based Acoustic Diode, Phys. Rev. Lett. **106**, 084301 (2011).

[31] M. Notomi, K. Yamada, A. Shinya, J. Takahashi, C. Takahashi, and I. Yokohama, Extremely Large Group-Velocity Dispersion of Line-Defect Waveguides in Photonic Crystal Slabs, Phys. Rev. Lett. **87**, 253902 (2001).

[32] T. F. Krauss, Slow light in photonic crystal waveguides, J. Phys. D: Appl. Phys. **40**, 2666 (2007).

[33] A. Imhof, W. L. Vos, R. Sprik, and A. Lagendijk, Large Dispersive Effects Near the Band Edges of Photonic Crystals, Phys. Rev. Lett. **83**, 2942 (1999).

[34] A. Cicek, O. Adem Kaya, M. Yilmaz, and B. Ulug, Slow sound propagation in a sonic crystal linear waveguide, J. Appl. Phys. **111**, 013522 (2012).

[35] F.-L. Hsiao, C.-Y. Hsieh, H.-Y. Hsieh, and C.-C. Chiu, High-efficiency acousto-optical interaction in phoxonic nanobeam waveguide, Appl. Phys. Lett. **100**, 171103 (2012).

[36] I. Psarobas, N. Papanikolaou, N. Stefanou, B. DjafariRouhani, B. Bonello, and V. Laude, Enhanced acousto-optic interactions in a one-dimensional phoxonic cavity, Phys. Rev. B **82**, 174303 (2010).

[37] K. F. Herzfeld and T. A. Litovitz, *Absorption and Dispersion of Ultrasonic Wave*, (Academic Press, New York & London, 2013), Vol. 7.

[38] F. E. Fox and G. D. Rock, Compressional viscosity and sound absorption in water at different temperatures, Phys. Rev. **70**, 68 (1946).

[39] J. Achenbach, *Wave Propagation in Elastic Solids* (Elsevier, Amsterdam, 2012).

[40] S. Benchabane, O. Gaiffe, R. Salut, G. Ulliac, V. Laude, and K. Kokkonen, Guidance of surface waves in a micron-scale phononic crystal line-defect waveguide, Appl. Phys. Lett. **106**, 081903 (2015).

[41] M. Ghasemi Baboly, C. M. Reinke, B. A. Griffin, I. ElKady, and Z. Leseman, Acoustic waveguiding in a silicon carbide phononic crystals at microwave frequencies, Appl. Phys. Lett. **112**, 103504 (2018).

[42] Y. Jin, N. Fernez, Y. Pennec, B. Bonello, R. P. Moiseyenko, S. Hémon, Y. Pan, and B. Djafari-Rouhani, Tunable waveguide and cavity in a phononic crystal plate by controlling whispering-gallery modes in hollow pillars, Phys. Rev. B **93**, 054109 (2016).

[43] Y.-F. Wang, T.-T. Wang, Y.-S. Wang, and V. Laude, Reconfigurable Phononic-Crystal Circuits Formed by Coupled Acoustoelastic Resonators, Phys. Rev. Appl. **8**, 014006 (2017).

[44] L. Rayleigh, On waves propagated along the plane surface of an elastic solid, Proc. London Math. Soc. **1**, 4 (1885).

[45] R. M. White and F. W. Voltmer, Direct piezoelectric coupling to surface elastic waves, Appl. Phys. Lett. **7**, 314 (1965).

[46] D. Yudistira, A. Boes, B. Djafari-Rouhani, Y. Pennec, L. Yeo, A. Mitchell, and J. Friend, Monolithic Phononic Crystals with a Surface Acoustic Band gap From Surface Phonon-Polariton Coupling, Phys. Rev. Lett. **113**, 215503 (2014).

[47] L. Socié, S. Benchabane, L. Robert, A. Khelif, and V. Laude, Surface acoustic wave guiding in a diffractionless high aspect ratio transducer, Appl. Phys. Lett. **102**, 113508 (2013).

[48] A. Khelif, Y. Achaoui, S. Benchabane, V. Laude, and B. Aoubiza, Locally resonant surface acoustic wave band gaps in a two-dimensional phononic crystal of pillars on a surface, Phys. Rev. B **81**, 214303 (2010).

[49] Y. Achaoui, A. Khelif, S. Benchabane, L. Robert, and V. Laude, Experimental observation of locally-resonant and bragg band gaps for surface guided waves in a phononic crystal of pillars, Phys. Rev. B **83**, 104201 (2011).

[50] S. Benchabane, O. Gaiffe, G. Ulliac, R. Salut, Y. Achaoui, and V. Laude, Observation of surface-guided waves in holey hypersonic phononic crystal, Appl. Phys. Lett. **98**, 171908 (2011).

[51] R. Wilson, J. Reboud, Y. Bourquin, S. L. Neale, Y. Zhang, and J. M. Cooper, Phononic crystal structures for acoustically driven microfluidic manipulations, Lab Chip **11**, 323 (2011).

[52] S. Brûlé, E. Javelaud, S. Enoch, and S. Guenneau, Experiments on Seismic Metamaterials: Molding Surface Waves, Phys. Rev. Lett. **112**, 133901 (2014).

[53] F.-C. Huang, Y.-Y. Chen, and T.-T. Wu, A room temperature surface acoustic wave hydrogen sensor with Pt coated ZnO nanorods, Nanotechnology **20**, 065501 (2009).

[54] A. Salman, O. A. Kaya, and A. Cicek, Determination of concentration of ethanol in water by a linear waveguide in a 2-dimensional phononic crystal slab, Sens. Actuator A-Phys. **208**, 50 (2014).

[55] R. Lucklum, M. Ke, and M. Zubtsov, Two-dimensional phononic crystal sensor based on a cavity mode, Sens. Actuator B-Chem **171**, 271 (2012).

[56] H.-S. Hong, D.-T. Phan, and G.-S. Chung, High-sensitivity humidity sensors with ZnO nanorods based two-port surface acoustic wave delay line, Sens. Actuator B-Chem. **171**, 1283 (2012).

[57] M. Kurosawa, Y. Fukuda, M. Takasaki, and T. Higuchi, A surface acoustic wave gyro sensor, Sens. Actuator A-Phys. **66**, 33 (1998).

[58] K. Jose, W. Suh, P. Xavier, V. Varadan, and V. Varadan, Surface acoustic wave MEMS gyroscope, Wave Motion **36**, 367 (2002).

[59] H. Oh, K. J. Lee, K. Lee, and S. S. Yang, Gyroscopes based on surface acoustic waves, Micro Nano Syst. Lett. **3**, 1 (2015).

[60] M. V. Gustafsson, T. Aref, A. F. Kockum, M. K. Ekström, G. Johansson, and P. Delsing, Propagating phonons coupled to an artificial atom, Science **346**, 207 (2014).

[61] R. Manenti, A. F. Kockum, A. Patterson, T. Behrle, J. Rahamim, G. Tancredi, F. Nori, and P. J. Leek, Circuit quantum acoustodynamics with surface acoustic waves, Nat. Commun. **8**, 975 (2017).

[62] X. Ding, P. Li, S.-C. S. Lin, Z. S. Stratton, N. Nama, F. Guo, D. Slotcavage, X. Mao, J. Shi, F. Costanzo, et al., Surface acoustic wave microfluidics, Lab Chip **13**, 3626 (2013).

[63] J. A. Stotz, R. Hey, P. V. Santos, and K. H. Ploog, Coherent spin transport through dynamic quantum dots, Nat. Mater. **4**, 585 (2005).

[64] S. Weis, R and K. gaylord, lithium niobate: Summary of physical properties and crystal structure, Appl. Phys. A **37**, 191 (1985).

[65] S.-Y. Yu, X.-C. Sun, X. Ni, Q. Wang, X.-J. Yan, C. He, X.-P. Liu, L. Feng, M.-H. Lu, and Y.-F. Chen, Surface phononic graphene, Nat. Mater. **15**, 1243 (2016).

[66] H. Jin, J. Zhou, X. He, W. Wang, H. Guo, S. Dong, D. Wang, Y. Xu, J. Geng, J. K. Luo, and W. I. Milne, Flexible surface acoustic wave resonators built on disposable plastic film for electronics and lab-on-a-chip applications, Sci. Rep. **3**, 2140 (2013).